Available online at www.sciencedirect.com
SCIENCE DIRECT
International Journal of Heat and Mass Transfer 49 (2006) 4577–4583
International Journal of HEAT and MASS TRANSFER
www.elsevier.com/locate/ijhmt

Initial growth of electrohydrodynamic instability of two-layered miscible fluids in T-shaped microchannels

Kwan Hyoung Kang [a,*], Jaewan Park [a], In Seok Kang [b], Kang Y. Huh [a]

[a] Department of Mechanical Engineering, Pohang University of Science and Technology, San 31, Hyoja-dong, Pohang 790-784, South Korea
[b] Department of Chemical Engineering, Pohang University of Science and Technology, San 31, Hyoja-dong, Pohang 790-784, South Korea

Received 30 November 2004; received in revised form 3 April 2006
Available online 30 June 2006

Abstract

A numerical analysis is performed for the electroosmotic flow of two miscible electrolyte streams in a T-shaped microchannel. Rich dynamic features are revealed concerning the onset and growth of the electrohydrodynamic instability. It is shown the molecular diffusion has dual role in the onset and development of instability, and the system is unstable to high electric fields even without any external disturbances. The molecular diffusion process is shown to play a key role in making the wave pattern looks regular and deterministic. Detailed mechanisms in the latter stage of instability growth and formation of spike-like wave patterns are also explained.

Keywords: Microchannel; Eletroosmotic flow; Instability; Interface; Numerical analysis

1. Introduction

In a microfluidic condition, fluid flow is usually stable due to the dominant role of viscous damping, and mixing liquids is actually like trying to stir molasses into honey [1]. In the respect of such a general nature of micro flows, flow instability observed in a T-channel by Chen et al. [2] and Shin et al. [3] may be considered as an interesting and extraordinary phenomenon. According to their observations, the two co-flowing layers with different electrolyte concentrations driven by DC [2] or AC [3] electroosmotic flow result in fast growth of wavy interfacial patterns as shown in Fig. 1. This kind of flow instability can be troublesome in proper functioning of some microfluidic devices requiring stable transport of species, such as in isoelectric focusing devices (Ref. [4] and references therein). On the other hand, this instability can be beneficially utilized as a means to promote mixing in microfluidic systems [5–7] (see, for more detailed review, Ref. [8]).

As explained by Lin et al. [8], this kind of instability can be categorized into a family of electrohydrodynamic instability. The conductivity or concentration gradient in an electric field is a source of electrical free charges, on which the Coulombic force may act to generate electrohydrodynamic flow. Hoburg and Melcher [9] showed that this type of polarization leads to unstable motion of two miscible contacting fluids of different concentrations under a parallel electric field to the interface in an unbounded domain. Baygent et al. [4] explained the origin of flow generated in isoelectric focusing devices in the same respect.

Santiago and his co-workers performed linear analysis and numerical analysis to understand the details of the instability [8,10–12]. Lin et al. [8] extended the analysis of Hoburg and Melcher [9] by including the advective effects due to electroosmotic flow. A linear and a nonlinear numerical analysis were performed, which exhibits a qualitative agreement to their experimental results. Storey et al. [11] demonstrated via a three-dimensional linear analysis that the top and bottom walls of a shallow channel stabilized the flow with respect to two-dimensional predictions. Chen et al. [12] preformed a more rigorous analysis for the

* Corresponding author. Tel.: +82 54 279 2187; fax: +82 54 279 3199.
E-mail address: khkang@postech.edu (K.H. Kang).

0017-9310/$ - see front matter © 2006 Elsevier Ltd. All rights reserved.
doi:10.1016/j.ijheatmasstransfer.2006.04.026

Nomenclature

c	molar concentration
D	diffusivity of ionic species
d	channel width
$\mathbf{E}$	electric field
F	Faraday constant
$\mathbf{i}$	current density
p	pressure
Pe	Peclet number, $u_c d/D = ReSc$
Sc	Schmidt number, ν/D
t	time
Re	Reynolds number, $u_c d/\nu$
$\mathbf{u}$	velocity vector
u_c	characteristic velocity, $u_c = \varepsilon\zeta_{ave}E_0/(2\mu)$
u_{HS}	Helmholtz–Smoluchowski slip velocity
V	external voltage
x	horizontal coordinate
y	vertical coordinate

Greek symbols

ε	electrical permittivity
ϕ	electrostatic potential
μ	fluid viscosity
ν	kinematic viscosity of fluid
ρ	fluid density
ρ_e	free charge density
σ	electrical conductivity
ω	ionic mobility
ζ	zeta potential
ζ_{ave}	average zeta potential, $(\zeta(c_l) + \zeta(c_h))/2$

Subscripts

+	cationic species
−	anionic species
h	higher concentration
l	lower concentration

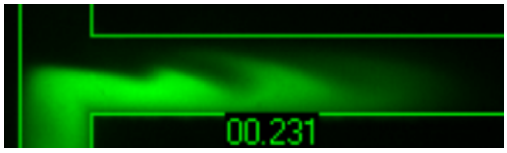

Fig. 1. Instability of electroosmotically-driven two-layered flow of aqueous NaCl solution having different concentrations. (Photo courtesy of S.M. Shin).

instability, and compared their prediction on temporal growth rate, threshold electric field for onset of instability, and so on, with their experimental results.

In all of those analyses, the temporal stability analysis is carried out, and any geometrical effects except the channel width cannot be considered. In addition, a white noise is "artificially" imposed as an initial condition, which eventually shows a rather chaotic growth of the instability waves. According to the previous observations for a T-shaped channel [2,3,12], however, the instability waves shows well organized features which is quite different from the case of straight channel considered in Refs. [8,10–12] (see Lin et al. [8]). For example, the wave pattern observed is very regular, and the overall structure of the spiky patterns is has mutually consistent patterns in all the experiments. It suggests that there exists unknown system-born and "deterministic" factors that induce the instability and govern the evolution of the instability.

In the present work, we specifically consider the instability in the T-shaped microchannel which corresponds to the experimental conditions in Refs. [2,3,12]. The specific objective is to find out the system-born factors with respect to a rather practical condition. We performed a numerical analysis for the two-dimensional unsteady DC electroosmotic flow, following the general methodology of Lin et al. [8]. The numerical analysis reproduces all the features of the instability waves observed in the experiments quite satisfactorily.

We found that, in a practical channel, the instability is initiated due to a diffusion-induced symmetry-breaking process occurring at the initial contact region of the two electrolyte streams. Thus, the system is unstable to a high external electric field even without any external disturbances. It is demonstrated that the molecular diffusion around the junction region of the two streams enhances the "spatial" development of the instability. In fact, the molecular diffusion has been known to just suppress the onset and development of instability by reducing the electrical body force [8,10–12]. It is also shown that the molecular diffusion process at the junction region plays a key role in making the wave pattern looks regular and deterministic.

2. Formulations

The domain of analysis is depicted in Fig. 2. The vertical and horizontal branches in the figure are called here the vertical and the horizontal channels respectively. The concentrations of the two electrolyte liquids entering the domain are indicated as c_h and c_l, in which h and l denote the high and low concentrations. We consider the case of 1:1 symmetric electrolyte. The electrolytes are free from chemical reaction and their activity coefficient is assumed to be unity. The dielectric constant of the solution is uniform throughout the domain. The thickness of the electrical double layer on walls is assumed to be much thinner than the channel width. These assumptions are reasonable and consistent with the previous experimental conditions [2,3].

All the material properties are assumed uniform in liquid and solid region, respectively. In the quasi-electro-

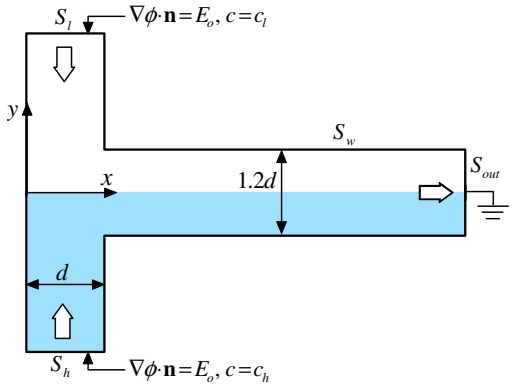

Fig. 2. Domain of analysis.

static limit, the electric field is separable from the magnetic field, and the Maxwell equations are simplified to [13,14]

$$\nabla\cdot(\varepsilon\mathbf{E})=\rho_e \tag{1}$$

$$\nabla\times\mathbf{E}=0 \tag{2}$$

$$\frac{\partial\rho_e}{\partial t}+\nabla\cdot\mathbf{i}=0 \tag{3}$$

where $\mathbf{E}=-\nabla\phi$ is the electric field, ϕ the electrostatic potential, ε electrical permittivity, ρ_e the free charge density, t the time, and $\mathbf{i}$ the current density.

For an electrolyte, the current is due to the motion of ionic species. The current density can be expressed as [15]

$$\mathbf{i}=-\sigma\nabla\phi-F(D_+\nabla c_- - D_+\nabla c_-)+F\mathbf{u}(c_+-c_-) \tag{4}$$

where $\sigma=F^2(\omega_++\omega_-)c$ is the conductivity, ω the mobility of the ionic species, F the Faraday constant, and c the molar concentration of electrolyte. In the above equation, the first, second, and third terms are the conduction, diffusion, and electromigration terms, respectively.

In an electrolytic system, the diffusional and convectional currents are in general negligible compared to the conductional current [14,16]. Then, the current density can be expressed by the Ohm's law of $\mathbf{i}=\sigma\mathbf{E}$. If there is no chemical reaction and no generation of ionic species, the conservation of species at a point requires

$$\frac{\partial c}{\partial t}+\mathbf{u}\cdot\nabla c=D\nabla^2 c \tag{5}$$

where $D=2D_+D_-/(D_++D_-)$ is the equivalent diffusivity.

In Eq. (3), under a DC electric field, the displacement current, $\partial\rho_e/\partial t$, can be neglected for a microscale scale system [13,14,16]. Then, the electrostatic potential satisfies

$$\nabla\cdot(\sigma\nabla\phi)=0 \tag{6}$$

Due to the quasi-electroneutrality assumption [14–16], we use the preceding equations rather than the Poisson equation, Eq. (1), to analyze the electric field. The Poisson equation is used for "after-the-fact" evaluation of the free charge density as follows:

$$\rho_e=-\frac{\varepsilon\nabla c\cdot\mathbf{E}}{c} \tag{7}$$

For an unsteady incompressible flow, the continuity and the momentum equation are written as

$$\nabla\cdot\mathbf{u}=0 \tag{8}$$

$$\rho\frac{D\mathbf{u}}{Dt}=-\nabla p+\mu\nabla^2\mathbf{u}+\rho_e\mathbf{E} \tag{9}$$

Here, $D/Dt=\partial/\partial t+\mathbf{u}\cdot\nabla$, p the pressure, ρ the mass density, and μ the viscosity of fluid.

Under the thin electrical double layer assumption, we take the Helmholtz–Smoluchowski slip velocity, u_{HS}, as the slip velocity on the wall, u_t [15], i.e.,

$$u_t=u_{HS}=-\frac{\varepsilon\zeta\mathbf{E}\cdot\mathbf{t}}{\mu}\quad\text{on } S_w \tag{10}$$

in which $\mathbf{t}$ is the unit tangential vector on the wall and ζ is the zeta potential of the wall. According to the experimental result of Shin et al. [3], the zeta potential is well approximated for NaCl solution in the range of 0.1 mM to 10 mM, by the following formula

$$\zeta(c)=7.8\times10^{-3}+2.1\times10^{-2}\log c \tag{11}$$

The initial conditions for concentration and momentum equations are given as follows:

$$\text{At}\quad t=0: c=c_l \text{ if } y>0, \text{ and } c=c_h \text{ if } y<0;\quad \mathbf{u}=\mathbf{0}, \text{ throughout the domain} \tag{12}$$

The boundary conditions for concentration, electric potential, and momentum equations are summarized as follows:

$$\text{On } S_l:\quad c=c_l;\ \nabla\phi\cdot\mathbf{n}=E_0;\ u=0,\ v=v_l \tag{13a}$$

$$\text{On } S_h:\quad c=c_h;\ \nabla\phi\cdot\mathbf{n}=E_0;\ u=0,\ v=v_h \tag{13b}$$

$$\text{On } S_w:\quad \nabla c\cdot\mathbf{n}=0;\ \nabla\phi\cdot\mathbf{n}=0;\ \mathbf{u}\cdot\mathbf{n}=0,\ \mathbf{u}\cdot\mathbf{t}=u_{HS} \tag{13c}$$

$$\text{On } S_{out}:\quad \nabla c\cdot\mathbf{n}=0;\ \phi=0;\ \mathbf{u}\cdot\mathbf{n}=0 \tag{13d}$$

Here, $\mathbf{n}$ is the outward unit normal at the boundary surface. Note that the constant flux condition of $\nabla\phi\cdot\mathbf{n}=E_0$ is applied on S_l and S_h.

We non-dimensionalize the equations by introducing the following non-dimensional variables:

$$\bar{t}=\frac{t}{t_c},\quad \bar{x}=\frac{x}{d},\quad \bar{y}=\frac{y}{d},\quad \bar{\mathbf{E}}=\frac{\mathbf{E}}{E_0},\quad \bar{\phi}=\frac{\phi}{E_0 d},$$
$$\bar{\mathbf{u}}=\frac{\mathbf{u}}{u_c},\quad \bar{c}=\frac{c}{c_h-c_l},\quad \bar{\rho}_e=\frac{\rho_e}{\varepsilon(E_0/d)}.$$

We take the average inlet velocity at S_l and S_h as the characteristic velocity of $u_c=\varepsilon\zeta_{ave}E_0/(2\mu)$, where $\zeta_{ave}=[\zeta(c_l)+\zeta(c_h)]/2$. The characteristic time is chosen as $t_c=d/u_c$. By substituting the dimensionless variables into Eqs. (5), (6), and (9), we obtain the following non-dimensional equations, in which the overbar is dropped for brevity:

$$\frac{D\mathbf{u}}{Dt} = -\nabla p + \frac{1}{Re}\nabla^2\mathbf{u} + \lambda(\nabla^2\phi)\nabla\phi \tag{14}$$

$$\nabla\cdot(c\nabla\phi) = 0 \tag{15}$$

$$\frac{Dc}{Dt} = \frac{1}{Pe}\nabla^2 c \tag{16}$$

Here, $Re = u_c d/\nu$, $Sc = \nu/D$ and $Pe = u_c d/D = ReSc$, are the Reynolds number, Schmidt number, and Peclet number. The parameter, $\lambda = \varepsilon E_0^2/(\rho u_c^2) = \mu^2/(\rho\varepsilon\zeta_{ave}^2)$, represents the relative magnitude of the Coulombic force with respect to the inertia force.

Let us consider the case of aqueous NaCl solution in a microchannel in which $d = 150\ \mu m$, $c_l = 1$ mM, $c_h = 10$ mM, $\varepsilon = 6.9\times10^{-10}$ C^2/(Jm), and $D = 1.5\times10^{-9}$ m^2/s. Then, it becomes $\zeta_l = -55.2$ mV, $\zeta_h = -34.2$ mV, $\zeta_{ave} = 44.7$ mV and $u_c = 0.93$ mm/s. In Fig. 1, the potential difference between the inlet and outlet is 700 V and the total length of the channel is about 1.7 cm. The electric field at S_l and S_h is estimated as $E_0 = 32$ kV/m. Then, the dimensionless parameters become $Re = 0.14$, $Pe = 87$, $Sc = 622$, and $\lambda = 819$.

3. Results and discussion

3.1. Numerical results and the mechanism of free charge generation

A numerical analysis is performed, on the basis of the finite volume method, for the fully coupled set of nonlinear equations of Eqs. (14)–(16), under the given initial and boundary conditions of Eqs. (12) and (13). The governing equations are discretized under the second-order upwind scheme. The SIMPLE method is used for pressure correction. A uniform rectangular mesh is used, in which $\Delta x = \Delta y = 0.04$. The time-step size is fixed at $t = 0.01$ for the unsteady simulation.

Fig. 3a shows the concentration distribution obtained numerically for $Re = 0.14$, $Pe = 87$, and $\lambda = 130$ in which four hump-shaped pattern (what we call hump) are clearly shown. Note that the concentration is inversely proportional to darkness level, and therefore, the concentration is higher at brighter region (lower part in Fig. 3a). Eight marker points (P1–P8) are placed for easier understanding

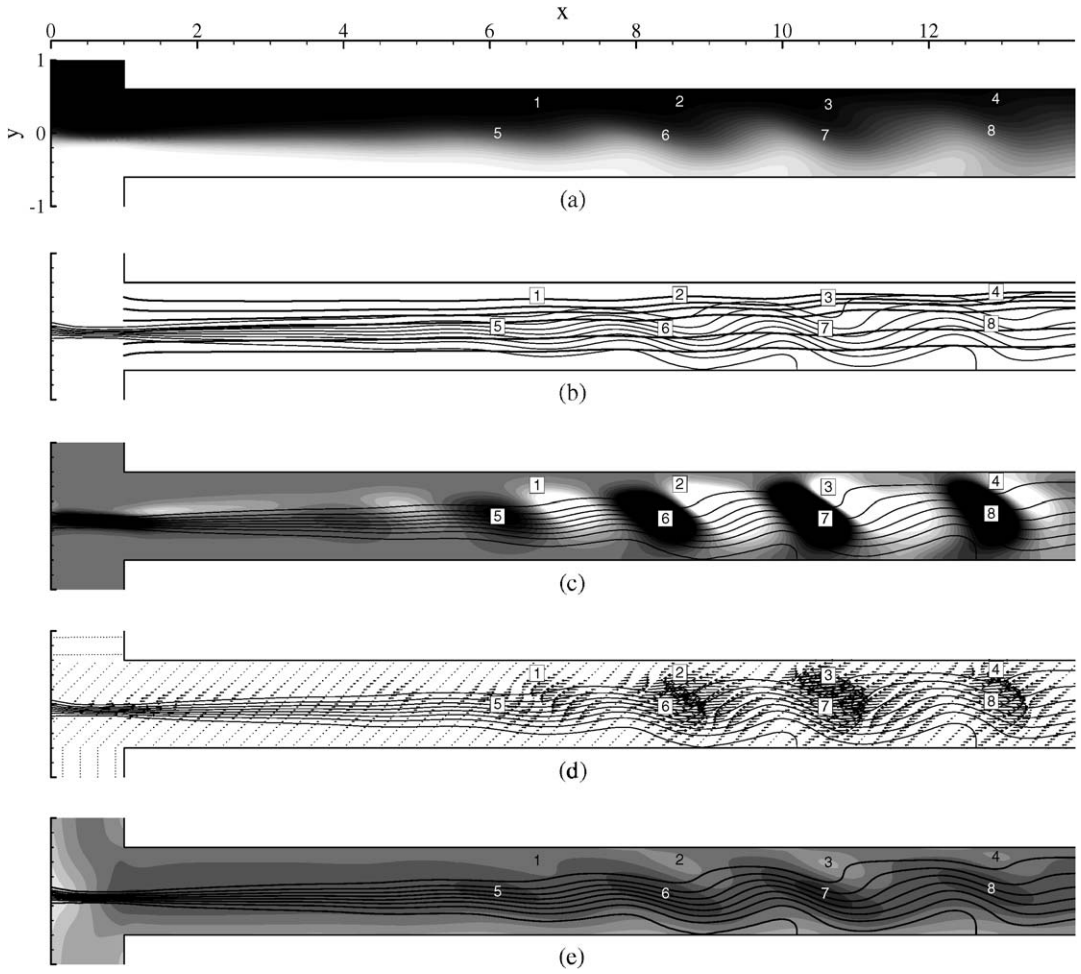

Fig. 3. Numerical results at an instant for $\lambda = 130$. (a) Concentration, (b) electric field line (thick line) and iso-concentration line (thin line), (c) free charge density with concentration (solid line), (d) Coulombic force vector ($\rho_e\mathbf{E}$, arrow), (e) magnitude of velocity vector (darkness level is proportional to velocity magnitude) and iso-concentration line (line).

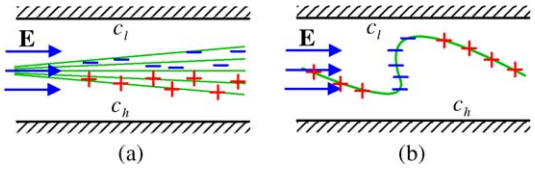

Fig. 4. Mechanisms of free charge generation. (a) diffusion, (b) interface deformation. "+" and "−" signs indicate the positive and negative charges.

in the figures. The amplitude of the humps grows as they are convected downstream. The overall interface patterns look similar to those from experimental results. Fig. 3b shows the electric field line, which becomes nearly straight just after the juncture region. Thus, the electric field is almost parallel to the horizontal axis in $1.5 < x < 5$. Fig. 3c shows the distribution of free charge density. The darkness level indicates the magnitude of positive charges, while the brightness is proportional to the magnitude of negative charges.

First, the free charge can be generated by the transverse diffusion of species (see Fig. 4a). It is supposed in Fig. 4a that the electric field is parallel to x-direction. The thickness of the mixing layer increases in the downstream direction due to convection and transverse diffusion. This results in a non-vanishing value of $\nabla c \cdot \mathbf{E}$. At the upper part of the mixing layer $\partial c/\partial x > 0$, while at the lower part $\partial c/\partial x < 0$. Accordingly, $\rho_e = -\varepsilon \nabla c \cdot \mathbf{E}/c < 0$ above the center region, and $\rho_e > 0$ below the center region. It will be discussed in the next section that this mechanism plays a crucial role in the onset and initial growth of instability.

On the other hand, the mechanism depicted in Fig. 4a is not the only way to generate the free charge by transverse diffusion. The tranverse diffusion for instance may influence the electric field by way of changing the conductivity distribution. (In the following section, we will show in Figs. 6 and 7 that the transverse diffusion affects the electric field distribution significantly). Hence, even when $\partial c/\partial x = 0$, free charge can be generated only if $\partial c/\partial y \times E_y \neq 0$, where E_y represents the vertical component of $\mathbf{E}$. The mechanism in Fig. 4a should be understood as a representative means to generate free charge by tranverse diffusion.

Second, the free charge is induced by interface deformation (see Fig. 4b). It is supposed also in Fig. 4b that the electric field is parallel to x-direction. If the interface is deformed due to some reason, which we will discuss later in this paper, $\nabla c \cdot \mathbf{E}$ becomes non-zero. The lower stream has a high concentration. As showin in Fig. 4b, therefore, $\nabla c \cdot \mathbf{E} > 0$ at the fore of a hump and $\nabla c \cdot \mathbf{E} < 0$ at the back of a hump. As a result, Fig. 3c shows $\rho_e < 0$ at the fore of each hump (close to P1–P4), while $\rho_e > 0$ and at the back of the hump (near P5–P8).

Fig. 3d shows the Coulombic force vectors. Fig. 3e shows the magnitude of velocity vector (contour). In Fig. 3e, the darkness level is proportional to the magnitude of the velocity vectors. High velocity regions are formed at the back of each hump (P5–P8), while low velocity regions

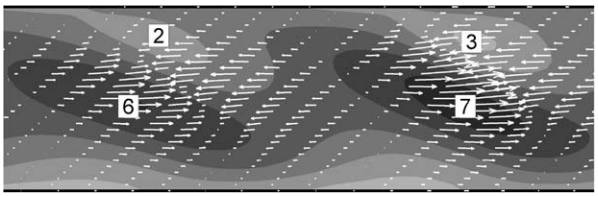

Fig. 5. Enlarged plot of Coulombic force vectors and magnitude of velocity vector shown in Fig. 3.

are formed at the front part. Fig. 5 shows the Coulombic force vectors and magnitude of velocity vector which are shown in Fig. 3d and Fig. 3e, respectively. We can find from Fig. 5 that the Coulombic force is directed to the positive (negative) x-direction at the high (low) velocity region. It is because the Coulombic force exerts force on fluid element. Accordingly, flow velocity would be increased around the region where the Coulombic force is directed to positive x-direction, and vice versa. Although not shown here, we verified that the fluctuation velocity vector (velocity vectors obtained by subtracting the x-directional mean velocity from the total velocity) quite resembles the Coulombic force vector.

3.2. Initial growth of the instability driven by transverse molecular diffusion

To demonstrate the effect of molecular diffusion, the free charge density and Coulombic force around the juncture region are compared for the two Peclet numbers of $Pe = 87$ and $Pe = 870$ in Figs. 6 and 7. In Figs. 6b and

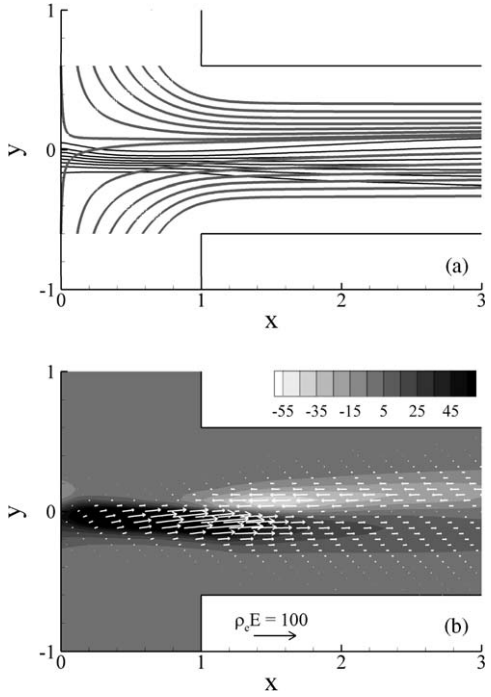

Fig. 6. Effect of diffusivity on free charge generation for $\lambda = 130$ and $Pe = 87$. (a) Concentration (thin black line) with electric field line (thick gray line). (b) Free charge density (contour) and Coulombic force ($\rho_e \mathbf{E}$, arrow). A reference vector is shown at the bottom of (b).

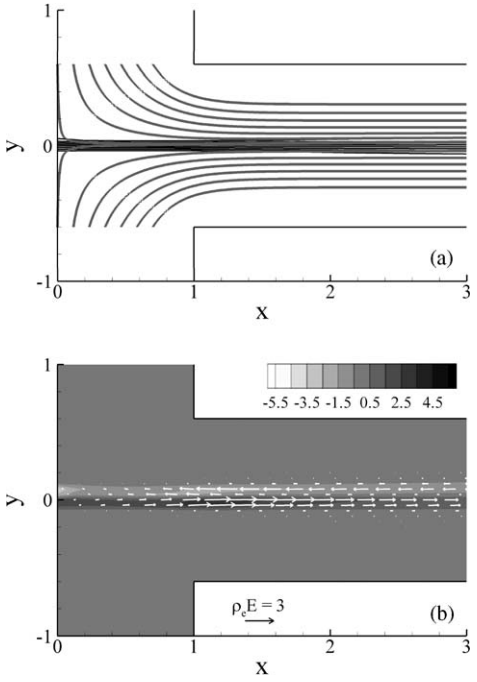

Fig. 7. $\lambda = 130$ and $Pe = 870$. (see Fig. 6 for figure caption).

7b, the darkness level indicates the magnitude of positive charges, while the brightness is proportional to the magnitude of negative charges. Note that the case of $Pe = 87$ corresponds to the previous case of Fig. 3. When diffusion rate is lower ($Pe = 870$), the fluid interface remains almost flat throughout the domain and no sign of instability is observed.

When $Pe = 87$, shown in Fig. 6, the electric field is rather deflected towards the upper wall. Moreover, the fluid interface near the left wall of the vertical channel is shifted downward. They are surely originated from the transversal-diffusion-induced charge depicted in Fig. 4a. As the molecular diffusion becomes significant, the magnitude of induced charge near the juncture region increases. Consequently, if we compare Figs. 6 and 7, the magnitude of free charge density and Coulombic force are roughly one order of magnitude greater for the case of $Pe = 87$. From this result, we can infer that as the diffusivity of the ions gets smaller, the amount of free charge would be reduced and onset of instability would be delayed.

For the two cases in common, a decelerating (accelerating) force acts on the upper (lower) part from the centerline in which $\rho_e < 0$ ($\rho_e > 0$). Thus, the fluid experiences a sort of counter-clockwise angular momentum near the juncture region. This angular momentum would deform the fluids interface. When $Pe = 870$, this momentum is not strong enough to cause the observable deformation of interface. When $Pe = 87$, however, the deceleration at the upper part and acceleration at the lower part eventually shift the interface to the downward direction due to the mass conservation. We checked that the shift becomes significant in proportion to the applied field strength, which is consistent to the experimental results of Shin et al. [3].

As shown, the effect of diffusion is so dramatic on the onset of instability. It is also interesting that the molecular diffusion plays a dual role in the generation of instability. If the molecular diffusion is sufficiently high, ∇c will be reduced at the downstream part, which reduces the growth rate of instability.

3.3. Later stage of growth driven by interface deformation

Fig. 3b shows the electric field lines and the concentration contours together. At the region around $1 < x < 6$, the electric field line and the concentration contour are quite parallel. This implies that ∇c and $\mathbf{E}$ may be orthogonal to each other, and $\nabla c \cdot \mathbf{E}$ may have a rather small value in this region. On the other hand, at the region of $x > 6$, the concentration contours are significantly deflected due to interface deformation, while the electric field lines still keeps quite straight forms compared to the concentration contour. It is evident that $\nabla c \cdot \mathbf{E}$ may have a large value in the region of $x > 6$. Accordingly, the magnitude of the induced charge will be proportional to the degree of interface deformation.

On the other hand, the Coulombic force either decelerates or accelerates fluid locally depending on the sign of charges. As shown in Figs. 3c and 4b, the negative and positive charges are induced periodically at the left-hand side and right-hand side of each hump. Therefore, flow velocity is decreased at the back of hump (P1–P4) and is increased at the fore (P5–P8) as shown in Fig. 3e. Accordingly, the interface will be further deformed by the action of Coulombic force on the free charge generated by interface deformation.

In summary, the interface deformation causes and enhances the generation of free charge while the existence of free charge may in turn causes interface deformation. Therefore, the free charge density and interface deformation has some feedback relationship. This relation eventually generates the spike-like interface patterns shown in Fig. 1. Note that the electrically-generated angular momentum is always in counter-clockwise direction for the present configuration. Consequently, the direction of spike is always backward which is consistent to previous experimental results.

Although it is not shown here, we performed numerical analyses by changing λ for the conditions of $Re = 0.14$ and $Pe = 87$. The instability started to grow within the domain of interest between $\lambda = 100$ and 110. In the experiment of Fig. 1, however, the instability was observed (within the domain of interest) at about $\lambda = 424$. The numerical analysis, therefore, under-predicts the threshold condition for electric-field strength by about half. It is fairly satisfactory considering that the fluid flow, electric field, and diffusion in the experiment have the three-dimensional characters.

4. Conclusions

The simulation reproduces important features of the interface patterns observed in experiments. This reconfirms

clearly that this electrohydrodynamic instability originates from polarization induced by a conductivity gradient in two mixing electrolyte layers. Initial disturbance is produced automatically by the molecular diffusion of species across the interface. Thus, the system is always unstable to the high external electric field even without external disturbances. It is demonstrated that the molecular diffusion around the junction region of the two streams enhances the spatial development of the instability. In turn, the occurrence of instability is delayed substantially in domain of interests when the molecular diffusion is very slow. It is also shown that the molecular diffusion process at the junction region plays a key role in making the wave pattern looks regular and deterministic. The initial perturbation formed in the vicinity of the T-junction grows explosively at the downstream part assisted by the deformation-induced polarization.

Acknowledgements

The present investigation was supported by the Brain Korea 21 Program in 2003. I.S.K. was also supported by a grant from the Center for Ultramicrochemical Process Systems sponsored by KOSEF.

References

[1] J. Knight, Microfluidics: Honey, I shrunk the lab, Nature 418 (2002) 474–475.
[2] C.H. Chen, H. Lin, S.K. Lele, J.G. Santiago, Electrokinetic microflow instability with conductivity gradients, in: Proceedings of μTAS2003, Squaw Valley, CA, 2003.
[3] S.M. Shin, I.S. Kang, Y.K. Cho, G.B. Lim, Instability of electroosmotic flow under a time-periodic electric field, in: Proceedings of the 2003 Ann. Meet. of AIChE, San Francisco, CA, 2003, Paper No. 2941.
[4] J.C. Baygents, F. Baldessari, Electrohydrodynamic instability in a thin fluid layer with an electrical conductivity gradient, Phys. Fluids 10 (1998) 302–311.
[5] A.O. El Moctar, N. Aubry, J. Batton, Electro-hydrodynamic microfluidic mixer, Lab. Chip. 3 (2003) 273–280.
[6] J. Park, S.M. Shin, K.Y. Huh, I.S. Kang, Application of electrokinetic instability for enhanced mixing in various micro-T-channel geometries, Phys. Fluids 17 (2005) 118101.
[7] S.M. Shin, I.S. Kang, Y.-K. Cho, Mixing enhancement by using electrokinetic instability under time-periodic electric field, J. Micromech. Microeng. 15 (2005) 455–462.
[8] H. Lin, B.D. Storey, M.H. Oddy, C.-H. Chen, J.G. Santiago, Instability of electrokinetic microchannel flows with conductivity gradients, Phys. Fluids 16 (2004) 1922–1935.
[9] J.F. Hoburg, J.R. Melcher, Internal electrohydrodynamic instability and mixing of fluids with orthogonal field and conductivity gradients, J. Fluid Mech. 73 (1976) 333–351.
[10] M.H. Oddy, J.G. Santiago, Multiple-species model for electrokinetic instability, Phys. Fluids 17 (2005) 064108.
[11] B.D. Storey, B.S. Tilley, H. Lin, J.G. Santiago, Electrokinetic instabilities in thin microchannels, Phys. Fluids 17 (2005) 018103.
[12] C.-H. Chen, H. Lin, S.K. Lele, J.G. Santiago, Convective and absolute electrokinetic instability with conductivity gradients, J. Fluid Mech. 524 (2005) 263–303.
[13] D.A. Saville, Electrohydrodynamics: the Taylor–Melcher leaky dielectric model, Ann. Rev. Fluid Mech. 29 (1997) 27–64.
[14] J.R. Melcher, Continuum Electromechanics, The MIT Press, Cambridge Massachusetts, 1981 (Chapter 2).
[15] R.F. Probstein, Physicochemical Hydrodynamics, second ed., John Wiley & Sons, New York, 1994.
[16] A. Castellanos, A. Ramos, A. González, N.G. Green, H. Morgan, Electrohydrodynamics and dielectrophoresis in microsystems: scaling laws, J. Phys. D: Appl. Phys. 36 (2003) 2584–2597.